Applications in Engineering Science 14 (2023) 100128

Contents lists available at ScienceDirect

Applications in Engineering Science

journal homepage: www.elsevier.com/locate/apples

Hindered thermal warping triggers tensile cracking in the cores of compressed columns of a fire-loaded tunnel segment structure: Efficiency and accuracy of beam theory prediction, compared to FEM

Maximilian Sorgner [a], Rodrigo Díaz Flores [a], Hui Wang [b], Christian Hellmich [a], Bernhard L.A. Pichler [a,*]

[a] Institute for Mechanics of Materials and Structures, TU Wien (Vienna University of Technology), Karlsplatz 13/202, 1040 Vienna, Austria
[b] School of Naval Architecture, Ocean and Civil Engineering, Shanghai Jiao Tong University, Shanghai 200240, China

ARTICLE INFO

Keywords:
Moderate fire
Reinforced concrete columns
Thermal eigenstresses
Tensile cracking

ABSTRACT

The nonlinear Finite Element Method (FEM) is the current gold standard for the thermo-mechanical analysis of reinforced concrete structures. As an alternative, this paper is devoted to a model reduction strategy which reduces the CPU time by a factor of 500. This strategy combines Fourier series-based solutions for the thermal conduction problem, and thermo-elastic Timoshenko beam theory. Temperature histories known to be relevant for fire accidents enter series solutions quantifying the conduction of heat into a closed cell frame consisting of slabs, walls, and columns. Corresponding temperature profiles are translated into thermal eigenstrains. The latter are represented as the sum of three portions: (i) their cross-sectional averages (called thermal eigenstretches); (ii) their cross-sectional moments (called thermal eigencurvatures); and (iii) the remaining eigenstrain distributions (called eigenwarping). The latter portion is hindered at the cross-sectional scale, giving rise to non-linearly distributed self-equilibrated thermal stresses. The eigenstretches and eigencurvatures, in turn, are constrained at the scale of the frame structure. Together with external mechanical loads, they enter the exact solutions of thermo-elastic Timoshenko beam theory with equivalent cross-sections accounting for the different material properties of concrete and steel. Axial normal stresses, quantified from beam-theory-related normal forces and bending moments, are superimposed with the hindered-warping-induced stresses. These stresses agree well with corresponding results obtained by the nonlinear FEM. As regards the load carrying behavior of the columns, excessive thermal tensile strains at the periphery of the columns trigger, in the core of the columns, large tensile stresses which even exceed the strength of concrete. Respective cracking events are considered through reduced effective columnar cross-sections. Right after initiation of cracking, around 12 min after the start of the heating process, the cracks propagate for some 30 sec quite rapidly, and very much slower thereafter. If the initial cross-sections of the columns are increased, more pronounced hindered thermal warping, together with less quickly evolving compressive forces, results in earlier cracking. Overall, it is concluded that tensile cracking is the key material non-linearity, at least during the first 30 min of the fire test, with maximum temperatures up to 300 °C.

1. Introduction

Exposure to fire may significantly challenge the structural integrity and stability of reinforced concrete structures. The corresponding challenges concerning design and maintenance are often tackled by means of devoted experimental campaigns, which may be accompanied or followed by corresponding simulation activities. Typically, measured and/or computed deflections and displacements of concrete members, such as beams, columns, or frames, are reported over some fire exposure time, typically ranging from 60 to 300 min (Terro, 1998; Zha, 2003; Kodur et al., 2003, 2004; Bratina et al., 2005; Xu and Wu, 2009; Han et al., 2009; Choi and Shin, 2011; Gao et al., 2013; Kodur et al., 2013; Ring et al., 2014a,b; Ožbolt et al., 2014; Albrifkani and Wang, 2016; Kodur et al., 2017). Comparatively, stress and strain distributions, typically computed by means of the Finite Element Method, are discussed much less, and are normally reported for time instants after a relatively long exposure duration, with the latter spanning from some 60 to 180 min (Han et al., 2009; Bratina et al., 2005; Gao et al., 2013; Ring et al., 2014b; Albrifkani and Wang, 2016). As a notable

* Corresponding author.
E-mail address: bernhard.pichler@tuwien.ac.at (B.L.A. Pichler).

https://doi.org/10.1016/j.apples.2023.100128
Received 3 June 2022; Received in revised form 16 January 2023; Accepted 9 February 2023
Available online 20 February 2023

complement to these contributions, Díaz et al. (2018) focused on tension-induced damage, which occurs already during the first 15 min of fire exposure; and they did so in the framework of non-linear 3D Finite Element analyses of reinforced concrete (RC) members used in tunnel engineering (Lu et al., 2019). While giving valuable insights into thermo-mechanical couplings in fire-exposed concrete structures, such FEM approaches remain rather CPU-intensive, in particular so if a reliable approximation of spatial stress and strain distributions is aimed at.

The present contribution presents a corresponding remedy, in form of a smart model reduction of the problem investigated by Díaz et al. (2018): A Fourier series-based solution of the thermal conduction problem is combined with elasto-brittle Timoshenko beam theory with damage-dependent cross-sectional properties. In this way, a drastic reduction of CPU time comes together with a trustworthy representation of thermal and mechanical strain and stress patterns emerging throughout the investigated slabs, walls, and columns.

In other words, the innovative aspect of the present investigation concerns the use of theoretical and computational tools beyond non-linear FE analyses reflecting cracking events inside the heated columns. While FE results will serve as a means of validation, the key contribution of the paper is a semi-analytical, beam-theory-based approach. The latter employs mechanically or thermally induced deformation patterns, such as stretching, bending, or warping, which are superimposed in a modular fashion. In addition to its high computational efficiency, this modular approach, contrary to the "all-in-one" FE approach, allows for identification of the key drivers of damage arising from fire exposure, and hence appears as a valuable complement to "all-in-one" approaches, such as FEM.

Accordingly, the remainder of the paper is structured as follows: After introduction of the investigated tunnel segment structure in Section 2, Fourier series-based solution of the transient heat conduction problem is covered in Section 3. Section 4 employs standard relations of beam theory, for relating axial normal stresses to normal forces and bending moments, as well as to thermally induced axial strains, stretches and curvatures. In Section 5, the beam model is complemented by the differential equilibrium equations for normal forces, shear forces, and bending moments, yielding thermo-elastic as well as thermo-elasto-brittle stress fields throughout the investigated structure. The latter are compared to FE results. Section 6 contains a structural variation analysis regarding the initial cross-section of the columns. Section 7 contains the discussion, before Section 8 closes the paper with conclusions drawn from the present study.

2. Statement of the thermo-mechanical structural problem

2.1. Monitored fire test on a tunnel segment structure made of reinforced concrete (Lu et al., 2019)

The fire-tested tunnel segment structure reported by Lu et al. (2019) exhibited a width of 5261 mm, a height of 1880 mm, and a depth of 1200 mm, see Fig. 1. In its core, it hosted two columns with rectangular cross-sections, 160 mm wide and 240 mm long. The structure was made of normal concrete "C40", with a mass density amounting to 2373 kg/m^3. The thickness of the concrete cover amounted to 30 mm. As for the reinforcement drawing see Fig. 3.

The reinforced concrete structure was placed sidelong on top of a furnace and closed with a fire-resistant cover, see Fig. 4. A steel frame was placed around the structure. It supported the tested structure, and it was equipped with hydraulic presses simulating ground pressure, see Fig. 1 for the geometric boundary conditions and for the locations of the external loads P_1, P_2, and P_3. Their intensities are listed in Table 1. Two heat sources produced the thermal loading. They were controlled such that the air temperature inside the furnace increased according to a pre-defined evolution. The one used by Lu et al. (2019) was the result of a statistical analysis of documented fire accidents, together with a

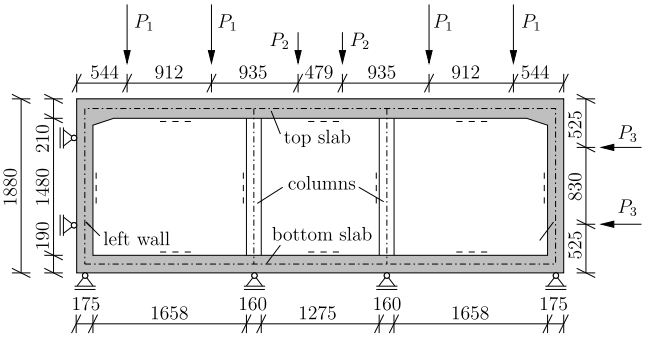

Fig. 1. Support conditions and mechanical loading of the structure tested by Lu et al. (2019); the dashed lines define the local coordinate systems as illustrated in Fig. 2.

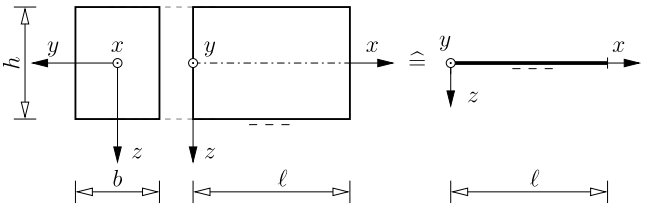

Fig. 2. Local coordinate systems describing positions inside and at the boundary of the structural elements: x denotes the local axial coordinate; y and z resolve the cross-sections.

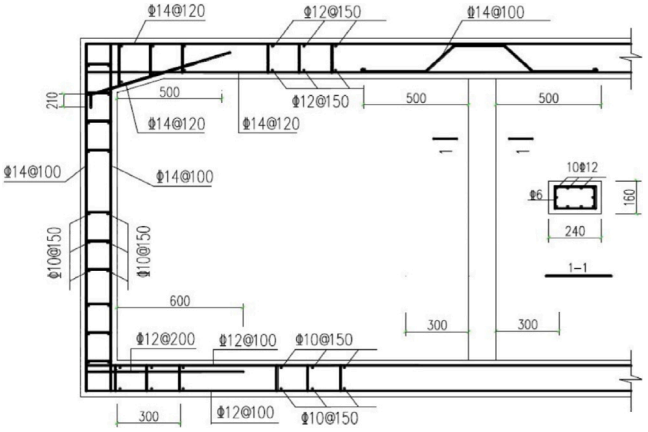

Fig. 3. Reinforcement drawing, after Lu et al. (2019).

Table 1
Intensities of the point loads imposed on the structure in order to simulate ground pressure (Lu et al., 2019).

	P_1	P_2	P_3
Force [kN]	192.0	151.2	120.0

simulation performed by a fire dynamics simulation software, which accounted for automatic sprinkler devices, a ventilation system, and an energy release rate of the heat source of 5 MW. In the first 30 min of the fire test, the air temperature increased to approximately 540 °C, which is about 300 °C lower than the temperature of the standard ISO 834 fire curve (International Organization for Standardization (ISO), 1999), see Fig. 5.

2.2. FE analyses of the monitored fire test (Díaz et al., 2018)

Díaz et al. (2018) simulated the fire test by means of three-dimensional, transient FE simulations (Dassault Systemes Simulia Corp,

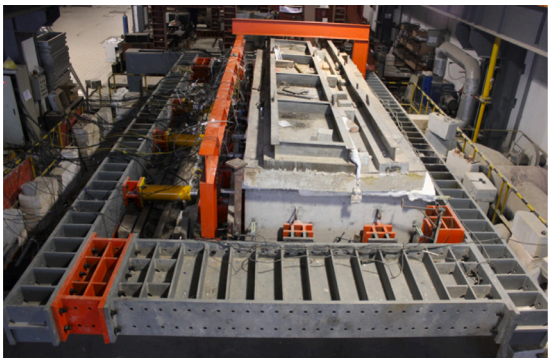

Fig. 4. Setup of the fire test, after (Lu et al., 2019).

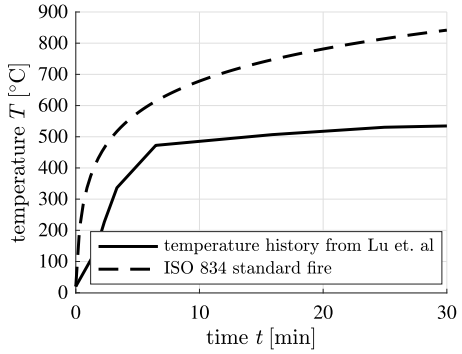

Fig. 5. Fire curves: the solid line refers to the one prescribed in the test by Lu et al. (2019), the dashed line to the ISO 834 standard fire (International Organization for Standardization (ISO), 1999).

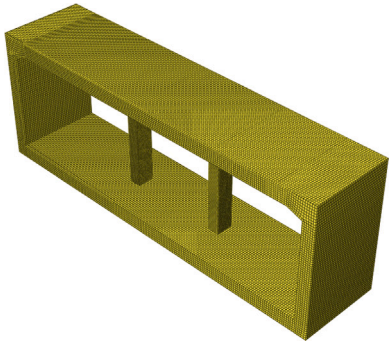

Fig. 6. Three-dimensional FE mesh, after (Díaz et al., 2018).

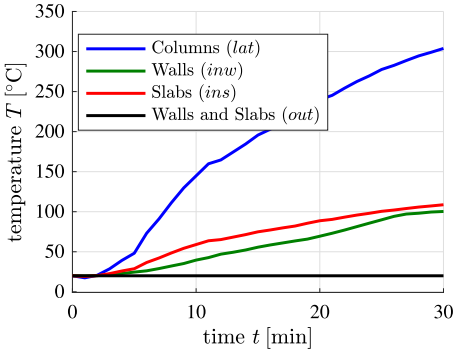

Fig. 7. Thermal boundary conditions: evolution of temperatures at the outer surfaces of the walls and slabs (*out*), their inner surfaces (*inw* and *ins*, respectively), and at the lateral surfaces of the columns (*lat*); after (Díaz et al., 2018).

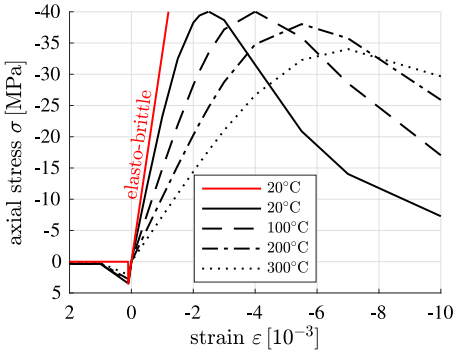

Fig. 8. Temperature-dependent stress–strain relations for concrete recommended by Eurocode 2 (black lines) and temperature-*in*dependent elasto-brittle stress–strain relation (red line), used in the FE simulation of Díaz et al. (2018) and the beam-theory-based approach of the present paper, respectively. (For interpretation of the references to color in this figure legend, the reader is referred to the web version of this article.)

Table 2
Thermo-mechanical properties of concrete and steel at room temperature; for their temperature-dependent evolutions see Fig. 8, and Figs. 16-18 in (Díaz et al., 2018).

Property	Concrete	Steel
Modulus of elasticity	$E_c = 33.4\,\text{GPa}$	$E_s = 195\,\text{GPa}$
Shear modulus	$G_c = 13.9\,\text{GPa}$	$G_s = 75\,\text{GPa}$
Poisson's ratio	$\nu_c = 0.2$	$\nu_s = 0.3$
Thermal expansion coefficient	$\alpha_c = 9.03 \times 10^{-6}\,1/°\text{C}$	$\alpha_s = 12.2 \times 10^{-6}\,1/°\text{C}$
Thermal diffusivity	$a_c = 0.749\,\text{mm}^2/\text{s}$	$a_s = 16.38\,\text{mm}^2/\text{s}$
Tensile strength / Yield stress	$f_t = 3.5\,\text{MPa}$	$f_y = 530\,\text{MPa}$

2019). The mesh consisted of 139,040 linear hexahedral brick finite elements "DC3D8", with characteristic sizes from 20 to 30 mm, eight nodes, and one temperature degree of freedom per node, see Fig. 6. The reinforcement bars were modeled as one-dimensional truss elements overlain to the concrete.

Prescribing, as boundary conditions, known surface temperature histories of the slabs, walls, and columns (Fig. 7) allowed for a satisfactory reproduction of temperature evolutions measured inside the structural elements (Díaz et al., 2018). Hence, the present study could do easily without computational fluid dynamics simulations of the heat transfer from the air to the surfaces of the structural elements. Since the columns were positioned in the vicinity of the two heat sources, they were heated faster than the other structural elements, see Fig. 7.

Two types of FE simulations were performed: (i) a linear elastic analysis accounting for thermo-mechanical properties of concrete and steel at room temperature, see Table 2, and (ii) an elasto-plastic analysis accounting for temperature-dependent and non-linear material behavior, see Fig. 8. These FE analyses provide twofold motivation for the present contribution:

1. Díaz et al. (2018) focused on cracks at the *surfaces* of the structural elements. In the present contribution, the main focus lies on the stress states *inside* the compressed columns.
2. The non-linear FE simulation was re-performed with a "ThinkPadT14s Gen1" (processor: Intel Core i7-10610U CPU@ 1.80GHz×8) and required a CPU time of 10.3 h. In order to achieve model reduction, a modular beam-theory-based approach is developed in the present contribution.

3. Solutions of transient heat conduction problems

Transient heat conduction is a boundary value problem. The field equation is the heat equation. Restricting the analysis to thermally

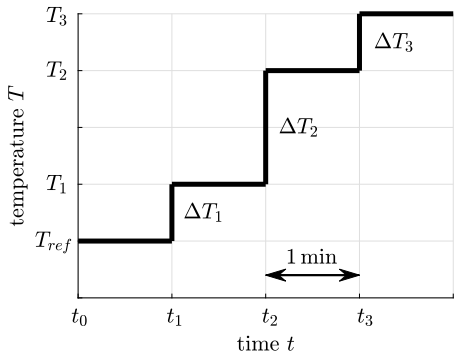

Fig. 9. Thermal boundary conditions at the surfaces of the structural elements: step-wise representation of the temperature histories of Fig. 7.

isotropic media and a Cartesian x, y, z-coordinate system, the heat equation reads as (Özısık, 1993)

$$\frac{\partial T}{\partial t} = a\left(\frac{\partial^2 T}{\partial x^2} + \frac{\partial^2 T}{\partial y^2} + \frac{\partial^2 T}{\partial z^2}\right), \tag{1}$$

where T denotes the temperature, a the thermal diffusivity, and t the time variable. The initial condition is isothermal at reference temperature

$$T_{ref} = 20\,^{\circ}\mathrm{C}\,. \tag{2}$$

As boundary conditions, the temperature histories of Fig. 7 are prescribed. They are represented in a step-wise fashion, see Fig. 9. The temperature steps at time t_k are quantified as

$$\Delta T_k^{pos} = T^{pos}(t_k) - T^{pos}(t_{k-1}), \quad \forall k = 1, 2, \ldots, 30\,. \tag{3}$$

where the time difference $t_k - t_{k-1}$ amounts to 1 min, and where the position indicator pos is equal to inw when analyzing the walls, ins when analyzing the slabs, and to lat when analyzing the columns.

The rebars have an insignificant influence on the heat conduction problem (Lie and Erwin, 1993). Therefore, the simulation of transient heat conduction through the structural elements is based on the values of the thermal diffusivity of concrete, rather than accounting for concrete and steel separately. The temperature of the rebars can be determined after the solution of the heat conduction problem. It is equal to the temperature of concrete in the immediate vicinity of the rebars.

3.1. One-dimensional heat conduction along wall and slab thicknesses

In the walls and slabs, heat is primarily conducted in the thickness direction, along which the local z-coordinates are measured. Thus, the heat equation (1) degenerates to

$$\frac{\partial T}{\partial t} = a\,\frac{\partial^2 T}{\partial z^2}\,. \tag{4}$$

The solution reads as (Wang et al., 2019)

$$\begin{aligned} T(z,t) = T_{ref} &+ \sum_{k=1}^{30} \Delta T_k^{pos}\left(\frac{1}{2} + \frac{z}{h}\right) \\ &+ \sum_{n=1}^{\infty} \exp\left(-\frac{(2n-1)^2\pi^2 a\langle t-t_k\rangle}{h^2}\right)\left[\frac{2\Delta T_k^{in}(-1)^n}{(2n-1)\pi}\cos\left((2n-1)\pi\frac{z}{h}\right)\right] \\ &+ \sum_{n=1}^{\infty} \exp\left(-\frac{(2n\pi)^2 a\langle t-t_k\rangle}{h^2}\right)\left[\frac{\Delta T_k^{in}(-1)^n}{n\pi}\sin\left(2n\pi\frac{z}{h}\right)\right], \end{aligned} \tag{5}$$

where ΔT_k^{pos} denotes the temperature steps at the inner surfaces of the walls ($pos = inw$) and slabs ($pos = ins$). They are computed according to Eq. (3), based on the temperature histories of Fig. 7. The angled brackets in (5) denote the Macaulay operator:

$$\langle t - t_k\rangle := \frac{1}{2}\left(t - t_k + |t - t_k|\right). \tag{6}$$

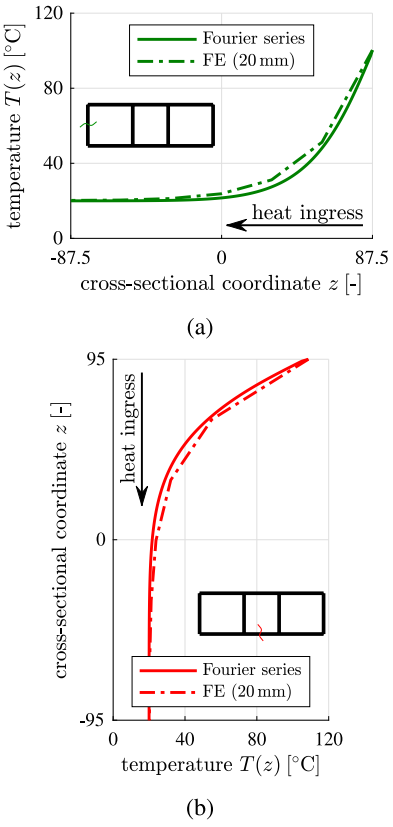

Fig. 10. Temperature profiles 30 min after the start of the fire of (a) the left wall, and (b) the bottom slab, obtained with the Fourier series approach, see the solid line, and with the regular FE model consisting of square-shaped elements with 20 mm side length, see the dash-dotted line.

The temperature profiles of the bottom slab and the walls obtained 30 min after the start of the fire agree well with corresponding results from the FE simulation, see Fig. 10. For the temperature profile of the top slab see (Sorgner et al., 2022).

3.2. Two-dimensional heat conduction across column cross-sections

In the columns, heat is primarily conducted within the cross-sections, in which the local y- and z-coordinates are measured. Thus, the heat equation (1) degenerates to

$$\frac{\partial T}{\partial t} = a\left(\frac{\partial^2 T}{\partial y^2} + \frac{\partial^2 T}{\partial z^2}\right). \tag{7}$$

The solution reads as

$$\begin{aligned} T(y,z,t) = T^{lat}(t) - \sum_{k=1}^{30}\sum_{m=0}^{\infty}\sum_{n=0}^{\infty} &\frac{16\,\Delta T_k^{lat}(-1)^{m+n}}{(2m+1)(2n+1)\pi^2} \\ &\cos\left(\frac{(2m+1)\pi}{h}z\right)\cos\left(\frac{(2n+1)\pi}{b}y\right) \\ &\exp\left(-\left(\left(\frac{2m+1}{h}\right)^2 + \left(\frac{2n+1}{b}\right)^2\right)\pi^2 a\langle t-t_k\rangle\right), \end{aligned} \tag{8}$$

where $\Delta T^{lat}(t)$ denotes the temperature at the lateral surface at time t and ΔT_k^{lat} denotes the temperature steps at the lateral surfaces of the column. They are computed according to Eq. (3), based on the temperature history of Fig. 7.

It is interesting to compare the Fourier series-based results according to Eq. (8), with the FE simulation results from a regular mesh of square-shaped constant strain elements with a side length of 20 mm, as reported in (Díaz et al., 2018). This is done for the temperature profiles in the middle of the columns, along the local y- and z-axes, see Fig. 11.

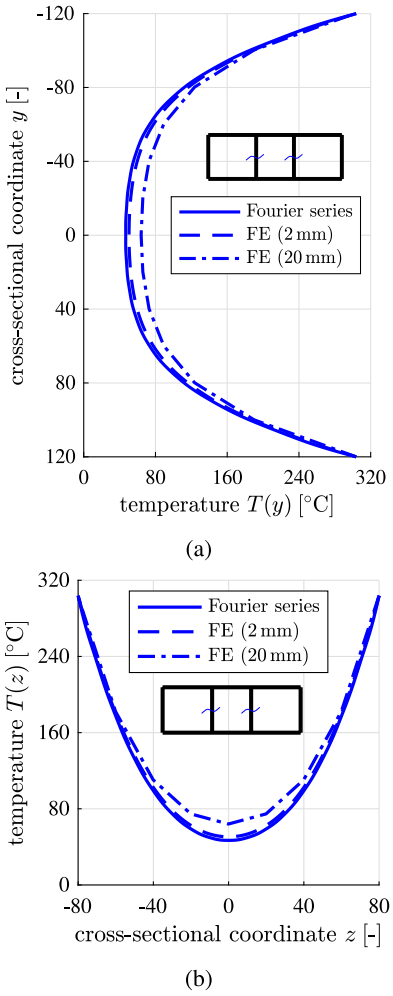

Fig. 11. Temperature profiles of the columns 30 min after the start of the fire along the local (a) y-axis and (b) z-axis, obtained with the Fourier series approach, see the solid lines, and with the FE models with regular meshes consisting of square-shaped elements with side lengths of 20 mm (Díaz et al., 2018), and of 2 mm, respectively; see the dash-dotted and dashed lines.

Near the lateral surfaces, the two differently computed temperature profiles agree well. At the center of the cross-section, the series solution according to Eq. (8) (solid line) suggests a temperature which is by 17.2 °C smaller than that obtained with the FE simulation (dash-dotted line). However, when performing a 2D simulation of heat conduction into the column, rather than performing a three-dimensional thermo-elastic simulation of the entire structure, it is straightforward (from the viewpoint of computational effort) to refine the FE mesh, e.g. from 20 mm to 2 mm element size. Corresponding FE results are much closer to those obtained with the series solution: the largest difference is smaller than 3.8 °C. Thus, the series solution agrees well with results from fine FE discretization. The two-dimensional temperature field illustrated in Fig. 12 serves as input for the following thermo-mechanical analysis.

4. Thermo-elasto-mechanics of reinforced concrete beams

All reinforced concrete members (walls, slabs, columns) will be mechanically represented as beams, with the local coordinate systems given in Fig. 2. Thermal loading of all these members leads to thermo-mechanical bending around their y-axes, see Fig. 2. All cross-sections exhibit double symmetry. They are composed of two materials: concrete and steel. This results in heterogeneous fields of the modulus of

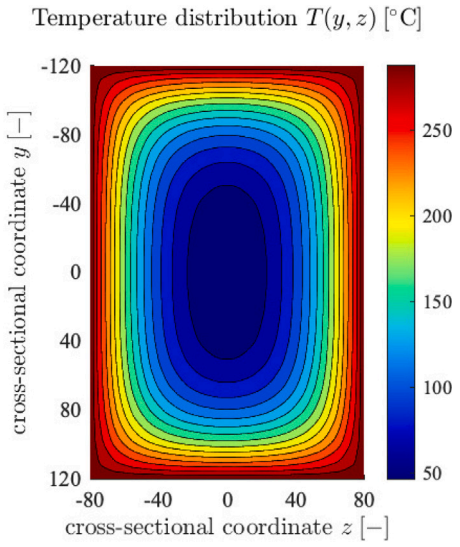

Fig. 12. Temperature distribution inside the cross-sections of the columns, 30 min after the start of the fire, obtained with series solution (8).

elasticity $E = E(y,z)$ and of the thermal expansion coefficient $\alpha = \alpha(y,z)$, where y and z denote Cartesian coordinates with origin at the axis of the beam, see Fig. 2. Double symmetric elastic distributions $E(y,z) = E(-y,z) = E(y,-z) = E(-y,-z)$ yield

$$\int_A E\, z \, \mathrm{d}A = \int_A E\, y \, \mathrm{d}A = 0\,. \tag{9}$$

In thermoelasticity, thermal stresses depend on the evolution of temperature relative to a reference temperature. In the case of beams with predominant heat flux in z-direction (walls and slabs) and in y- and z-directions (columns), this reads as

$$\Delta T(y,z,t) = T(y,z,t) - T_{ref}\,. \tag{10}$$

4.1. Thermal eigenstrains and axial normal stresses in heterogeneous beams

If a beam with heterogeneous cross-section is subjected to transient heat conduction, changes of temperature will be non-linearly distributed across the cross-section. Related eigenstrains are equal to the product of the thermal expansion coefficient, α, and the temperature change ΔT:

$$\varepsilon^e_{xx} = \varepsilon^e_{yy} = \varepsilon^e_{zz} = \alpha\, \Delta T\,. \tag{11}$$

At the cross-sectional scale, the eigenstrains (11) are subdivided into three portions: the eigenstretch and the eigencurvature of the axis of the beam, and the eigenwarping of its cross-section (Wang et al., 2022). In the following, it will be shown that rules for this decomposition follow from the Euler–Bernoulli hypothesis, stating that reinforced concrete cross-sections remain plane in the deformed configuration:

$$u = u_0 - \frac{\mathrm{d}w_0}{\mathrm{d}x}\, z\,, \tag{12}$$

where u stands for the axial displacement field of the cross-section, u_0 denotes the axial displacement of the center of gravity of the cross-section, and w_0 stands for its deflection. The axial normal stress reads as $\sigma_{xx} = E\,(\varepsilon_{xx} - \varepsilon^e_{xx})$, where E stands for the modulus of elasticity, and ε_{xx} denotes the axial normal strain. Expressing the latter as the partial derivative of u according to Eq. (12) with respect to x, yields

$$\sigma_{xx} = E\,(\varepsilon_0 + \kappa_0\, z - \varepsilon^e_{xx})\,, \tag{13}$$

with $\varepsilon_0 = \mathrm{d}u_0/\mathrm{d}x$ and $\kappa_0 = -\mathrm{d}^2 w_0/\mathrm{d}x^2$ denoting the stretch and the curvature of the axis of the beam. Insertion of Eq. (13) into the

expression for the normal force, $N = \int_A \sigma_{xx}\,\mathrm{d}A$, yields the constitutive law as

$$N = \overline{EA}\left(\varepsilon_0 - \varepsilon_0^e\right), \tag{14}$$

the effective extensional stiffness as

$$\overline{EA} = \int_A E\,\mathrm{d}A, \tag{15}$$

and the eigenstretch of the axis of the beam as

$$\varepsilon_0^e = \frac{1}{\overline{EA}}\int_A E\,\alpha\Delta T\,\mathrm{d}A, \tag{16}$$

with A denoting the cross-sectional area. Similarly, insertion of Eq. (13) into the expression for the bending moment, $M = \int_A \sigma_{xx}\,z\,\mathrm{d}A$, yields the constitutive law as

$$M = \overline{EI}\left(\kappa_0 - \kappa_0^e\right), \tag{17}$$

the effective bending stiffness as

$$\overline{EI} = \int_A E\,z^2\,\mathrm{d}A, \tag{18}$$

and the eigencurvature of the axis of the beam as

$$\kappa_0^e = \frac{1}{\overline{EI}}\int_A E\,\alpha\,\Delta T\,z\,\mathrm{d}A. \tag{19}$$

Solving Eq. (14) for ε_0 and Eq. (17) for κ_0 and inserting the resulting expressions into Eq. (13), yields the following expression for the stresses:

$$\sigma_{xx} = \frac{N\,E}{\overline{EA}} + \frac{M\,E}{\overline{EI}}\,z + \sigma_{xx}^e, \tag{20}$$

with the hindered-warping-induced stresses

$$\sigma_{xx}^e = -E\left[\alpha\Delta T - \varepsilon_0^e - \kappa_0^e\,z\right]. \tag{21}$$

4.2. Application to reinforced concrete members

The cross-section of a reinforced concrete member consists of concrete (index c) and steel rebars (index s). Their moduli of elasticity are denoted as E_c and E_s, respectively, the actual cross-sectional areas of concrete and steel as A_c and A_s, respectively.

The effective extensional stiffness according to Eq. (15) can be evaluated as

$$\overline{EA} = E_c\left[A_c + n_E\,A_s\right] = E_c A_{eq}, \tag{22}$$

where n_E stands for the ratio E_s/E_c, and A_{eq} for the area of the "equivalent" uniform concrete cross-section. Denoting the thermal expansion coefficients of concrete and steel as α_c and α_s, respectively, the change of temperature of the j^{th} rebar as ΔT_j, and its cross-sectional area as A_j, the eigenstretch (16) can be expressed as

$$\varepsilon_0^e = \frac{1}{A_{eq}}\left[\int_{A_c}\alpha_c\,\Delta T\,\mathrm{d}A + n_E\sum_{j=1}^{L}\alpha_s\,\Delta T_j\,A_j\right], \tag{23}$$

where L stands for the number of rebars.

The effective bending stiffness according to Eq. (18) can be evaluated as

$$\overline{EI} = E_c\left[I_c + n_E\,I_s\right] = E_c I_{eq}, \tag{24}$$

where I_c and I_s denote the second moments of inertia of the cross-sectional subareas occupied by concrete and steel, respectively. I_{eq} stands for the second moment of inertia of the "equivalent" uniform concrete cross-section. The eigencurvature (19) can be expressed as

$$\kappa_0^e = \frac{1}{I_{eq}}\left[\int_{A_c}\alpha_c\Delta T\,z\,\mathrm{d}A + n_E\sum_{j=1}^{L}\alpha_s\Delta T_j A_j z_j\right], \tag{25}$$

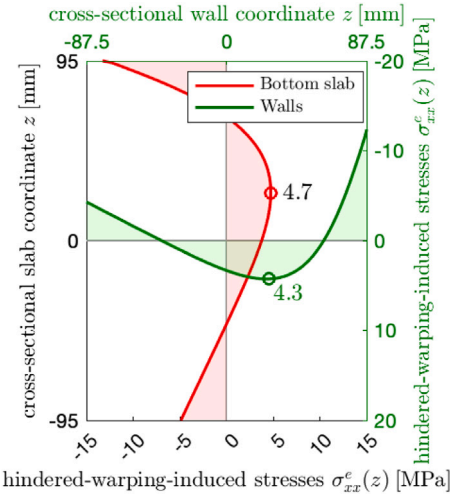

Fig. 13. Hindered-warping-induced stresses experienced by concrete of the left wall and the bottom slab, according to the third term on the right-hand-side of Eq. (26), 30 min after the start of the fire.

where z_j denotes the z-coordinate of the axis of the j^{th} rebar.

The expression for the stresses according to Eqs. (20) and (21) takes the form

$$\sigma_{xx,c} = \frac{N}{A_{eq}} + \frac{M}{I_{eq}}\,z - E_c\left[\alpha_c\Delta T - \varepsilon_0^e - \kappa_0^e\,z\right], \tag{26}$$

$$\sigma_{xx,s} = \frac{N\,n_E}{A_{eq}} + \frac{M\,n_E}{I_{eq}}\,z - E_s\left[\alpha_s\Delta T - \varepsilon_0^e - \kappa_0^e\,z_j\right]. \tag{27}$$

4.3. Eigenstretches, eigencurvatures, and hindered eigenwarping of the walls and slabs

Insertion of the temperature solution according to Eq. (5) into Eq. (10), and of the resulting expression into Eqs. (23) and (25) yields the eigenstretch and the eigencurvature of the reinforced concrete beams as

$$\varepsilon_0^e = \alpha_c\frac{A_c}{A_{eq}}\sum_{k=1}^{30}\Delta T_k^{in}\left[\frac{1}{2} - \sum_{n=1}^{\infty}\frac{4}{(2n-1)^2\pi^2}\exp\left(-\frac{(2n-1)^2\pi^2 a\langle t - t_k\rangle}{h^2}\right)\right] + n_E\,\alpha_s\sum_{j=1}^{L}\Delta T_j\frac{A_j}{A_{eq}}, \tag{28}$$

and

$$\kappa_0^e = -\alpha_c\frac{I_c}{I_{eq}}\sum_{k=1}^{30}\Delta T_k^{in}\left[\frac{1}{h} - \sum_{n=1}^{\infty}\frac{6}{(n\pi)^2}\frac{1}{h}\exp\left(-\frac{(2n\pi)^2 a\langle t - t_k\rangle}{h^2}\right)\right] + n_E\,\alpha_s\sum_{j=1}^{L}\Delta T_j\frac{A_j}{I_{eq}}\,z_j. \tag{29}$$

The eigenstretches and the eigencurvatures of the walls and the slabs, obtained 30 min after the start of the fire, are listed in Table 3.

The eigenwarping of the cross-sections of the walls and slabs is hindered. The resulting stresses of concrete, see Eq. (21) and the third term on the right-hand-side of Eq. (26), are computed according to the flowchart of Table 4, see Fig. 13. Their tensile maxima amount to 4.3 MPa and 4.7 MPa, respectively. These values are of the same order of magnitude as the tensile strength of concrete. However, these tensile stresses are reduced by compression in the structural elements, resulting from the point loads of Table 1, which were not considered in Fig. 13.

Table 3
Cross-sectional properties of the structural elements: "equivalent properties" refer to a fictitious cross-section consisting of concrete only, "real properties" refer to the actual concrete part of the actual cross-section, "ratio factors" are defined in Eq. (33), eigenstretches and eigencurvatures are defined in Eqs. (28)-(30), evaluated for $t = 30$ min.

	Cross-section b, h [mm]	Equivalent properties A_{eq} [mm^2], I_{eq} [mm^4]	Real properties A [mm^2], I [mm^4]	Equivalence ratios [−], see Eq. (33)	Eigenstretch & -curvature ε_0^e [−], κ_0^e [mm^{-1}]
Top slab	$b = 1000$ $h = 210$	$A_{eq} = 2.684 \times 10^5$ $I_{eq} = 1.019 \times 10^9$	$A = 2.520 \times 10^5$ $I = 9.261 \times 10^8$	$\eta_A = 1.065$ $\eta_I = 1.100$	$\varepsilon_0^e = 1.1848 \times 10^{-4}$ $\kappa_0^e = 2.4632 \times 10^{-6}$
Bottom slab	$b = 1000$ $h = 190$	$A_{eq} = 2.411 \times 10^5$ $I_{eq} = 7.415 \times 10^8$	$A = 2.280 \times 10^5$ $I = 6.859 \times 10^8$	$\eta_A = 1.058$ $\eta_I = 1.081$	$\varepsilon_0^e = 1.2860 \times 10^{-4}$ $\kappa_0^e = 2.8946 \times 10^{-6}$
Lateral wall	$b = 1000$ $b = 175$	$A_{eq} = 2.279 \times 10^5$ $I_{eq} = 5.953 \times 10^8$	$A = 2.100 \times 10^5$ $I = 5.359 \times 10^8$	$\eta_A = 1.085$ $\eta_I = 1.111$	$\varepsilon_0^e = 1.1362 \times 10^{-4}$ $\kappa_0^e = 2.7662 \times 10^{-6}$
Columns	$b = 240$ $h = 160$	$A_{eq} = 4.387 \times 10^4$ $I_{eq} = 9.291 \times 10^7$	$A = 3.840 \times 10^4$ $I = 8.192 \times 10^7$	$\eta_A = 1.143$ $\eta_I = 1.134$	$\varepsilon_0^e = 13.7000 \times 10^{-4}$ $\kappa_0^e = 0$

Table 4
Flowchart for the computation of $\sigma^e_{xx,c}$ for the walls, the slabs, and the columns according to Eq. (21).

1.	Define numerical values for the material and cross-sectional properties, see Table 2 and Table 5.
2.	Compute the area, A_{eq}, and the second moment of inertia, I_{eq}, of the equivalent cross-section according to Eqs. (34) and (35).
3.	Define the temperature steps at the heated surfaces according to Eq. (3), based on data from Fig. 7.
4.	Determine the eigenstretch ε_0^e and the eigencurvature κ_0^e according to Eqs. (28) and (29) for the walls and slabs, and according to Eq. (30) for the columns, respectively.
5.	Compute the temperature change in Eq. (10) under consideration of Eq. (5) for the walls and slabs, and Eq. (8) for the columns.
6.	Compute the third term in Eq. (26) for the hindered-warping-induced stresses of concrete.

4.4. Eigenstretches and hindered eigenwarping of the columns

Insertion of the temperature solution according to Eq. (8) into Eq. (10), and of the resulting expression into Eq. (23) yields the eigenstretch of the reinforced concrete columns as

$$\varepsilon_0^e(t) = \alpha_c \frac{A_c}{A_{eq}} \left[\Delta T^{lat} - \sum_{k=1}^{30} \sum_{m=0}^{\infty} \sum_{n=0}^{\infty} \frac{64\, \Delta T_k^{lat}}{(2m+1)^2 (2n+1)^2 \pi^4} \exp\left(-\left(\left(\frac{2m+1}{h} \right)^2 + \left(\frac{2n+1}{b} \right)^2 \right) \pi^2 a \langle t - t_k \rangle \right) \right] + n_E \sum_{j=1}^{L} \alpha_s \Delta T_j \frac{A_j}{A_{eq}} . \tag{30}$$

30 min after the start of the fire, the eigenstretch amounts to 13.7×10^{-4}. This is by one order of magnitude larger than the eigenstretches of the walls and slabs, see Table 3. The eigencurvature according to Eq. (25) vanishes because of the double-symmetric temperature field: $\kappa_0^e = 0$.

The eigenwarping of the cross-sections of the columns is hindered. The resulting stresses of concrete, see Eq. (21) and the third term on the right-hand-side of Eq. (26), are computed according to the flowchart of Table 4, see Fig. 14. Their tensile maximum amounts to 37.5 MPa. This is one order of magnitude larger than the tensile strength of concrete. In order to find out whether or not these tensile stresses are compensated by the point load-induced compressive normal forces in the columns, a structural analysis is required. It will be described next.

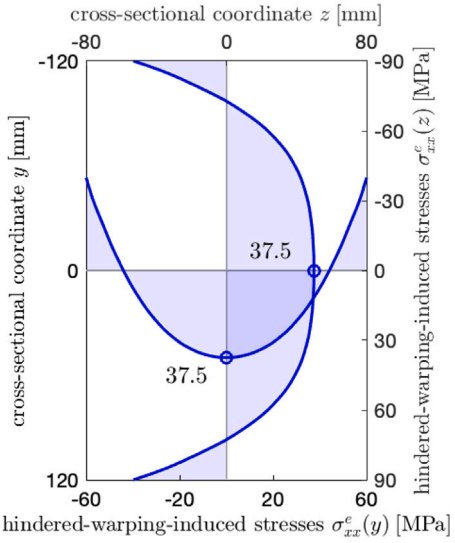

Fig. 14. Hindered-warping-induced stresses experienced by concrete of the columns, according to the third term on the right-hand-side of Eq. (26), 30 min after the start of the fire.

5. Structural analysis of the monitored fire test by Lu et al. (2019)

5.1. Timoshenko beam theory

Beam analysis software (Dlubal Software GmbH, 2020) is used to provide exact analytical solutions to the differential equations of Timoshenko beam theory (Elishakoff, 2020; Öchsner, 2021), including equilibrium conditions

$$\frac{\mathrm{d}V}{\mathrm{d}x} = -q\,, \quad \frac{\mathrm{d}M}{\mathrm{d}x} = V + m\,, \quad \frac{\mathrm{d}N}{\mathrm{d}x} = n\,, \tag{31}$$

and combined geometric-constitutive relations

$$\frac{\mathrm{d}w}{\mathrm{d}x} = \varphi + \frac{V}{G\tilde{A}}\,, \quad \frac{\mathrm{d}\varphi}{\mathrm{d}x} = -\left[\frac{M}{EI} + \kappa_0^e \right], \quad \frac{\mathrm{d}u}{\mathrm{d}x} = \frac{N}{EA} + \varepsilon_0^e\,. \tag{32}$$

For the present application, the transversal, axial, and rotational loads per unit length vanish: $q = n = 0$ kN/m and $m = 0$ kNm/m. In Eqs. (31) and (32), V denotes the shear force, and $G\tilde{A}$ the shear stiffness of the structural elements. For reinforced concrete members with rectangular cross-sections, it reads as $G\tilde{A} = (5/6)\, G_c A_{eq}$, where G_c is the shear modulus of concrete, see Table 2. Bending moments M and normal forces N resulting from the external point loads as well as

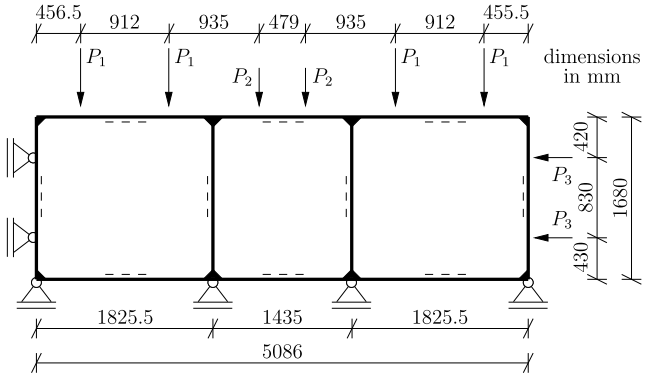

Fig. 15. Idealized representation of the tested segment of a subway station, as the basis for structural analysis using beam analysis software: for the numerical values of the point loads P_1, P_2, and P_3 see Table 1.

Table 5
Reinforcement properties of the structural elements: the "z-coordinate" refers to the distance of the axis of the rebar from the center of gravity of the reinforced-concrete cross-section, "number of rebars" refers to the number of rebars with the same z-coordinate, and "rebar area" refers to the cross-sectional area of each rebar.

	z-Coordinate z_j [mm]	Number of rebars	Rebar area A_j[mm^2]
Top slab	$z_j = -75$ $z_j = +75$	11	$A_j = 153.9$
Bottom slab	$z_j = -65$ $z_j = +65$	12	$A_j = 113.1$
Walls	$z_j = -58$ $z_j = +58$	12	$A_j = 153.9$
Columns	$z_j = -50$ $z_j = 0$ $z_j = +50$	4 2 4	$A_j = 113.1$

from the eigenstretches ε_0^e and the eigencurvatures κ_0^e of the structural elements (see Fig. 1 and Tables 1–3) are computed by means of an exact analytical solution of the differential equations of Timoshenko beam theory, see Eqs. (31) and (32). The analyzed structure is a closed-cell frame which is statically indeterminate to the twelfth degree. The dashed lines in Fig. 15 define the local coordinate systems, as illustrated in Fig. 2. The used beam analysis software requires, as input for every structural element, the ratios η_A and η_I, which are defined as:

$$\eta_A = \frac{A_{eq}}{A}, \qquad \eta_I = \frac{I_{eq}}{I}. \tag{33}$$

where $A = b\,h$ denotes the real cross-sectional area, and $I = bh^3/12$ the real second moment of inertia, see also Fig. 2. The equivalent properties of the reinforced concrete cross-sections read as

$$A_{eq} = A + (n_E - 1)\sum_{j=1}^{L} A_j\,, \tag{34}$$

$$I_{eq} = I + (n_E - 1)\sum_{j=1}^{L}\left(\frac{A_j^2}{4\pi} + A_j\,z_j^2\right), \tag{35}$$

where $n_E = E_s/E_c = 5.838$, see also Table 2. Two types of computations will be carried out. The first one refers to the point loads only, see Section 5.2. This simulation provides insight into the structural behavior *before* the start of the fire. The second type of computation refers to the point loads, the eigenstretches, and the eigencurvatures, representing the thermal loading 30 min *after* the start of the fire, see Section 5.3. The differences of the results of the two simulations, regarding the normal forces and bending moments, refer to load redistributions resulting from the fire.

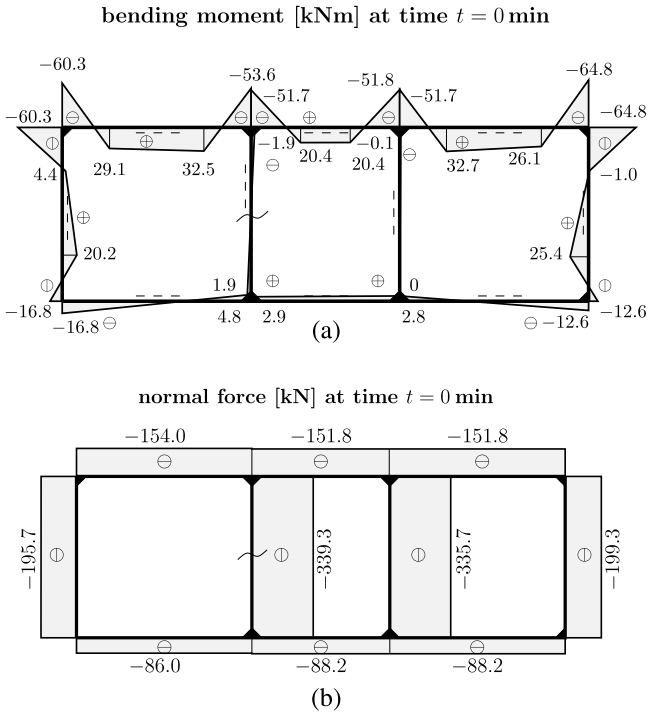

Fig. 16. Beam-theory-related stress resultants before the start of the fire, due to the point loads listed in Table 1: (a) bending moments, (b) normal forces.

5.2. Mechanical loading simulating ground pressure

The structural model is subjected to point loads P_1, P_2, and P_3, see Table 1. The obtained stress resultants (i.e. normal forces and bending moments) are virtually symmetric with respect to a column-parallel axis through the center of the structure, see Fig. 16.

The largest absolute values of the bending moments range from 52 kNm to 65 kNm. They are activated in the top slab, at the connections with the walls and the columns, see Fig. 16(a). The bending moments of the bottom slab are significantly smaller. Despite the rigid connections between the columns and the slabs, the bending moments in the columns are almost equal to zero.

The normal forces are negative and constant throughout every structural element, see Fig. 16(b). The normal force of the top slab is larger than that of the bottom slab. The largest compressive normal forces are activated in the columns. They amount to −339.3 kN and −335.7 kN, respectively.

5.3. Mechanical and thermal loading representative for a moderate tunnel fire

The structural model is subjected to point loads P_1, P_2, and P_3, see Table 1, and to eigenstretches and eigencurvatures representative for the time instant 30 min after the start of the fire, see Table 3. The obtained stress resultants are virtually symmetric with respect to a column-parallel axis through the center of the structure, see Fig. 17.

Because of the fire, the bending moments are significantly increased throughout the structure, compare Figs. 16(a) and 17(a). The largest absolute values of the bending moments range from 91 kNm to 181 kNm. They are activated in the top slab, at the connections with the walls and the columns, see Fig. 17(a). The bending moments of the bottom slab range from −66.8 kNm to −85.0 kNm. Despite the rigid connections between the columns and the slabs, the bending moments in the columns remain rather small.

The redistributions of the normal forces are governed by the eigenstretches of the columns, which are by one order of magnitude larger

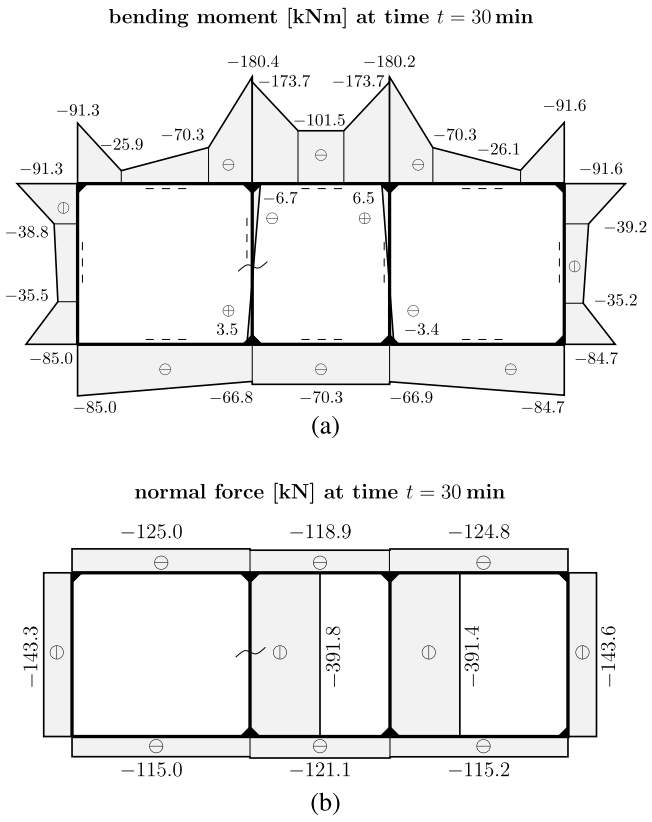

Fig. 17. Beam-theory-related stress resultants due to both the point loads listed in Table 1 and the fire-induced eigenstretches and eigencurvatures listed in Table 3: (a) bending moments, (b) normal forces.

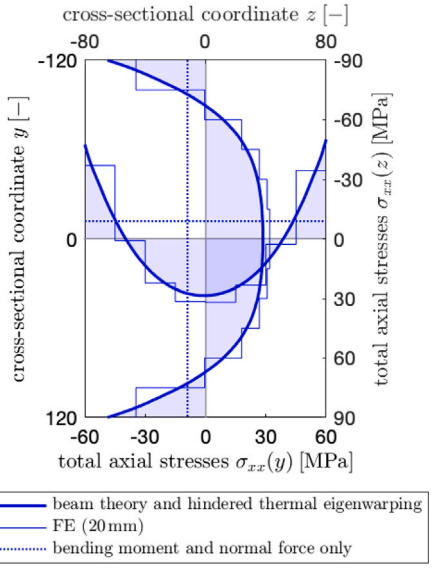

Fig. 18. Axial stresses along the local y- and z-axes at the half-height of the columns, 30 min after the start of the fire, obtained with the approach combining Timoshenko beam theory and Fourier series-defined non-linear temperature distributions (thick solid lines), with FE simulation (thin solid lines); the dotted lines refer to stresses resulting from external loads, as well as from thermal eigenstretches and eigencurvatures.

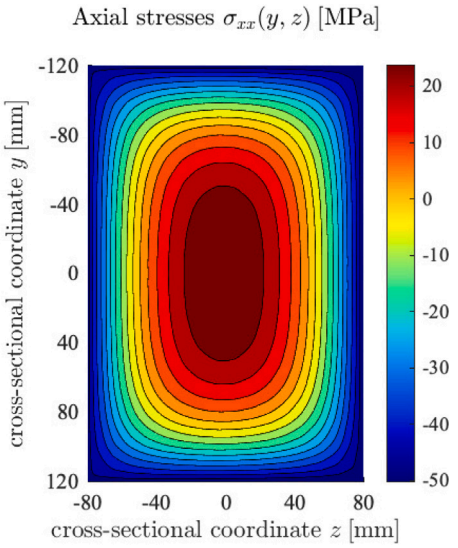

Fig. 19. Distribution of axial stresses across half-height cross section through left column; the result corresponds to the solid thick lines in Fig. 18.

than those of the walls. Because the expansion of the columns is constrained, their compressive normal forces rise, during the first 30 min of the fire, from −335 kN to −392 kN. This goes along with a reduction of the normal forces of the left wall from −196 kN to −143 kN, and of the right wall from −199 kN to −144 kN.

5.4. Total stresses at half-height of the left column, 30 min after the start of the fire

Axial stresses result, in every cross-section, from three contributions: the normal force N and the bending moment M (Fig. 17), as well as the hindered-warping-induced stresses, σ^e_{xx} (Fig. 14). The following analysis is focused on the cross-section at half-height of the left column, where the stress resultants read as $N = -391.8$ kN and $M = -1.6$ kNm. The normal force and the (vanishing) bending moment result in a uniform distribution of the axial normal stresses, see the dotted lines in Fig. 18. Adding the hindered-warping-induced stresses from Fig. 14, leads to non-linearly distributed total stresses, see the thick solid lines in Fig. 18. The solution for the total stresses, obtained with the described beam-theory-based approach, are compared with the stress distributions obtained from a linear elastic FE simulation, with temperature independent properties of concrete and steel. The FE-computed stresses are uniform within each element, because trilinear displacement shape functions were used. The element-wise uniform stresses agree quantitatively well with the smooth stress solution obtained from the beam model, see Fig. 18.

The linear-elastic analysis delivers an unreasonable result. The tensile axial normal stresses at the center of the cross-section of the column amount to 28.5 MPa. This is by one order of magnitude larger than the tensile strength of concrete at room temperature: $f_t = 3.5$ MPa. Unrealistically large tensile stresses are obtained in the core region of the cross-section, over some 80% of its height and 45% of its width, see Fig. 19. In order to improve this situation, brittle tensile failure will be considered inside the core regions of the columns, as described next.

5.5. Tensile cracking of the core of the columns

Tensile cracking is accounted for in cross-sectional planes of the columns, see the dark gray ellipses in Fig. 20. Determination of the axial spacing between these cracks is a complex task and an open research question. As a remedy, it is assumed that the crack spacing is so small that the material volume between two neighboring cracks (see the light gray domains in Fig. 20) does not experience significant stresses. This situation will be modeled by reducing, for all cross-sections along the entire length of the columns, the effective extensional and bending stiffness [defined by Eqs. (15) and (18)], such that the

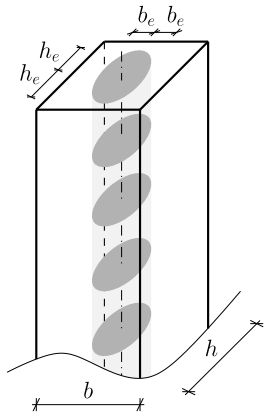

Fig. 20. Tensile cracking in elliptic domains around the centers of gravity of the columns.

updated values are representative of cracked cross-sections. In more detail, the following considerations are made:

Tension-induced cracking of concrete is modeled in elliptic domains around the centers of the columnar cross-section. This is motivated by the quasi-elliptic isolines of axial normal stresses in the innermost region of the cross-sections, see Fig. 19. Denoting the radius of the semi-major-axis (= y-axis) as h_e and that of the semi-minor-axis (= z-axis) as b_e, the elliptic domain is defined as:

$$\frac{y^2}{h_e^2} + \frac{z^2}{b_e^2} = 1\,. \tag{36}$$

The corresponding equivalent geometric properties read as

$$A_{eq}^{cr} = A_{eq} - h_e\, b_e\, \pi\,, \tag{37}$$

$$I_{eq}^{cr} = I_{eq} - \frac{\pi\, h_e\, b_e^3}{4}\,, \tag{38}$$

where the superscript cr stands for "cracked", and where A_{eq} and I_{eq} follow Eqs (34) and (35), see also Table 3. Numerical values of the semi-radii of the elliptic cracks, h_e and b_e, are determined iteratively, with the aim to obtain, along the contour of the crack, axial tensile stresses which are equal to the tensile strength of concrete; see Table 6. Before explaining the individual steps of this calculation, its result is anticipated:

$$h_e = 95.0\,\text{mm}\,, \tag{39}$$

$$b_e = 57.6\,\text{mm}\,. \tag{40}$$

Corresponding values of the equivalent cross-sectional area and the equivalent moment of inertia are listed in Table 7.

Heat conduction into the column is not affected by cracking, because concrete remains intact in between neighboring cracks, see Fig. 20. The material conducts heat in the two in-plane directions, as modeled in Section 3.2. Consequently, the temperature distribution inside the columns (Fig. 11) remains valid.

The spatial distribution of the thermal eigenstrains remains the same as in the case without cracking. However, the tensile eigenstrains in the cracked core region are now (virtually) *free to develop*. They reduce the opening widths of the cracks, but do not activate (significant) stresses. Eigenstrains in the intact (= non-cracked) outer part of the columns, in turn, are *constrained*. Therefore, they are subdivided into their stiffness–weighted mean value (= eigenstretch of the columns) and the spatially non-linear rest (= eigenwarping of the cross-section of the columns), as explained next.

The eigenstretch of the cracked columns is equal to the stiffness–weighted mean value of thermal eigenstrains in the intact (= non-cracked) outer region of the columns. Insertion of the temperature distribution from Eq. (8) into Eq. (10), and of the resulting expression

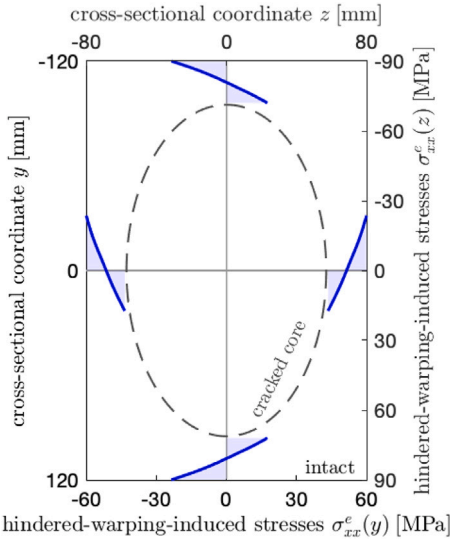

Fig. 21. Hindered-warping-induced stresses according to Eq. (21), along local y- and z-axes, at the half-height of the columns, 30 min after the start of the fire, under consideration of tensile cracking of the core region (dashed gray ellipse), obtained from the Fourier-series-defined non-linear temperature distributions (thick solid lines).

for the temperature change into Eq. (23), while limiting the integration over the outer intact area of the cross-section, yields

$$\begin{aligned}\varepsilon_0^{e,cr} = \frac{1}{A_{eq}^{cr}} \Bigg\{ A_{eq}\varepsilon_0^e - \Bigg[h_e b_e \pi\, \alpha_c \Delta T^{lat} \\ - \alpha_c \sum_{k=1}^{30} \sum_{m=0}^{\infty} \sum_{n=0}^{\infty} \frac{64 b\, \Delta T_k^{lat} (-1)^m}{(2m+1)^2 (2n+1) \pi^3} \\ \exp\left(- \left(\frac{(2n+1)^2}{b^2} + \frac{(2m+1)^2}{h^2} \right) a \pi^2 \langle t - t_k \rangle \right) \\ \int_0^{h_e} \cos\left(\frac{(2m+1)\,\pi}{h} z \right) \cos\left(\frac{(2n+1)\,\pi b_e}{b h_e} \sqrt{h_e^2 - z^2} \right) \mathrm{d}z \Bigg] \Bigg\},\end{aligned} \tag{41}$$

see Table 7 for the numerical result.

The eigenwarping of the cracked columns is equal to the total thermal eigenstrains in the intact outer part of the cross-sections minus the eigenstretch of Eq. (41), see also Table 7. This eigenwarping is hindered because the intact parts of the cross-sections remain plane according to the Bernoulli–Euler hypothesis.

The corresponding stresses are computed based on Eq. (21), see also the third term on the right-hand-side of Eq. (26). To this end, E_c and α_c are taken from Table 2. ΔT is computed according to Eq. (10) with $T(y,z,t)$ from Fig. 12 and T_{ref} from Eq. (2). ε_0^e in Eqs. (21) and (26) is set equal to $\varepsilon_0^{e,cr}$ from Table 7, and κ_0^e equal to $\kappa_0^{e,cr} = 0$. The resulting hindered-warping-induced stresses are self-equilibrated, i.e. their mean value vanishes. They are compressive in the outer region of the cross-sections, and they are tensile in the vicinity of the crack, see Fig. 21.

In order to compute the stresses resulting from the external loads as well as from the thermally induced eigenstretches and eigencurvatures, an updated structural analysis is performed. This simulation is carried out by means of beam analysis software (Dlubal Software GmbH, 2020), with the following input values: the extensional stiffnesses, the bending stiffnesses, the eigenstretches, and the eigencurvatures of the walls and the slabs are taken from Table 3, corresponding values of the cracked columns from Table 7, and the values of the point loads from Table 1. The obtained distributions of bending moments and normal forces are illustrated in Fig. 22. Dividing the normal force of the left column ($N = 401\,\text{kN}$, see Fig. 22) by the equivalent cross-sectional area of the cracked column ($A_{eq}^{cr} = 26673$ mm, see Table 7) delivers

Table 6
Flowchart for the computation of h_e and b_e according to Eqs. (39) and (40).

1.	Define initial numerical values for h_e and b_e.
2.	Compute A_{eq}^{cr} and I_{eq}^{cr} according to Eqs. (37) and (38).
3.	Compute the effective "cracked" column stiffnesses $\overline{EA}^{cr} = E_c A_{eq}^{cr}$ and $\overline{EI}^{cr} = E_c I_{eq}^{cr}$
4.	Determine the updated eigenstretch $\varepsilon_0^{e,cr}$ according to Eq. (41).
5.	Subject the structural model to point loads P_1, P_2, and P_3, see Table 1, and to eigenstretches and eigencurvatures representative for the time instant 30 min after the start of the fire, see Table 3, except for the columns, for which the updated eigenstretch is given in Eq. (41). Run a structural simulation, in order to compute the stress resultants (normal forces and bending moments).
6.	Determine the total concrete stresses in the outer intact part of the columns based on Eq. (26), in which $\overline{EA}$, $\overline{EI}$, ε_0^e, and κ_0^e are replaced by $\overline{EA}^{cr}$, $\overline{EI}^{cr}$, $\varepsilon_0^{e,cr}$, and 0, respectively.
7.	Stop algorithm if the tensile strength is reached at the intersections of the semi-major-axes with the crack edge.
8.	Increase the value of h_e, if the total tensile stresses at the intersection of the semi-major-axis (= y-axis) with the crack edge are larger than the tensile strength of concrete, and vice versa.
9.	Increase the value of b_e, if the total tensile stresses at the intersection of the semi-minor-axis (= z-axis) with the crack edge are larger than the tensile strength of concrete, and vice versa.
10.	Go back to step 2.

Table 7
Properties of cracked columns used for thermo-elasto-brittle analysis.

Property	Value
Equivalent area	$A_{eq}^{cr} = 26673\,\text{mm}^2$
Equivalent moment of inertia	$I_{eq}^{cr} = 78634000\,\text{mm}^4$
Ratio factor	$\eta_A^{cr} = 0.695$
Ratio factor	$\eta_I^{cr} = 0.960$
Eigenstretch	$\varepsilon_0^{e,cr} = 18.6 \times 10^{-4}$
Eigencurvature	$\kappa_0^{e,cr} = 0\,\text{mm}^{-1}$

uniformly distributed axial normal stresses experienced by concrete, which amount to −15.0 MPa, see the dotted lines in Fig. 23.

The total stresses of the left column, see Fig. 23, follow from the superposition of the stresses associated with the beam-theory-related normal forces and bending moments, (see the previous paragraph) with the hindered-warping-induced stresses, see Fig. 21. At the intersections of the crack contour with the y-axis and with the z-axis, respectively, the total stresses are tensile and amount to 3.49 MPa and 3.39 MPa, respectively. These values are close to the tensile strength of concrete. This underlines that the semi-radii of the cracks according to Eqs. (39) and (40) are realistic.

The beam theory solution was based on temperature-*in*dependent thermo-mechanical properties of concrete and steel, see Table 2. In addition, linear elastic material behavior was assumed for both concrete and steel, except for the tensile behavior of concrete, for which linear elastic behavior up to the tensile strength was assumed to be followed by brittle cracking. It is interesting to compare the obtained total stresses with those from a non-linear elasto-plastic FE simulation (Díaz et al., 2018). The latter was carried out with the "Concrete Damaged Plasticity" model (Dassault Systemes Simulia Corp, 2019) and accounted for both temperature-dependent thermo-mechanical properties *and* non-linear stress–strain relations of concrete and steel, see Figs. 16–18 in (Díaz et al., 2018). The element-wise uniform stresses obtained from the FE simulation, see the thin solid lines in Fig. 23, are quantitatively well reproduced with the smooth stress solution obtained from the much simpler, temperature distribution-informed beam-theory-based simulation, see the thick solid lines in Fig. 23. This underlines that the hindered-warping-induced stresses triggered tensile cracking of concrete inside the columns, while other material non-linearities and temperature-dependent properties of concrete and steel were of minor importance, at least during the first 30 min of the fire test, with maximum temperatures up to 300 °C.

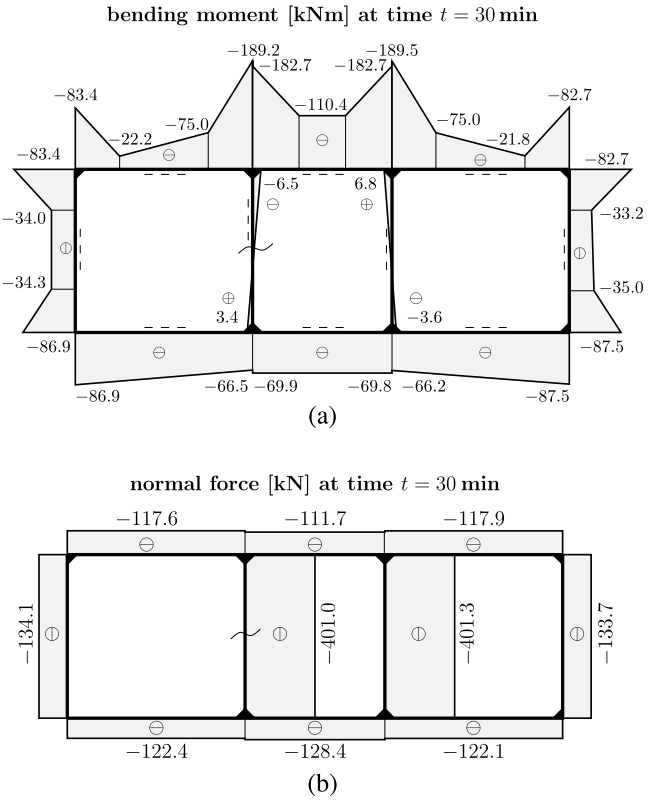

Fig. 22. Beam-theory-related stress resultants due to the point loads and the fire-induced eigenstretches and eigencurvatures, under consideration of tensile cracking of the core region of the columns: (a) bending moments, (b) normal forces.

5.6. *Evolution of cracking inside the columns*

The evolution of cracking of the columns is simulated throughout the first 30 min after the start of the fire. The analysis steps described for the beam-theory-based approach are repeated for several time instants. During the first 11 min after the start of the fire, the axial stresses inside the columns are smaller than the tensile strength of concrete. Thus, there is no need to simulate tensile cracking. 11.7 min after the

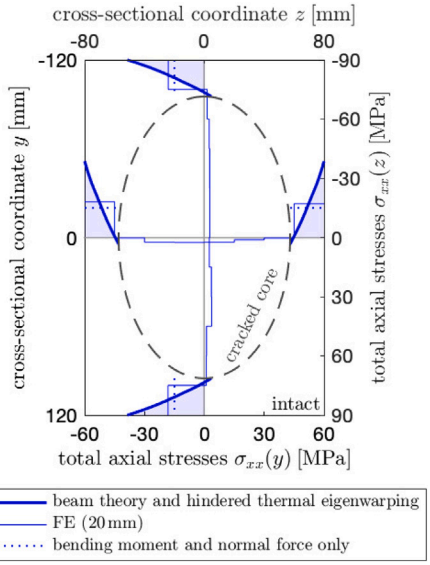

Fig. 23. Axial stresses along the local y- and z-axes at the half-height of the columns, 30 min after the start of the fire, under consideration of tensile cracking of the core region (dashed gray ellipse), obtained with the approach combining Timoshenko beam theory with Fourier series-defined non-linear temperature distributions (thick solid lines) and with the FE simulation (thin solid lines); the dotted lines refer to stresses resulting from external loading (point loads of Table 1) as well as from thermally induced eigenstretches and eigencurvatures.

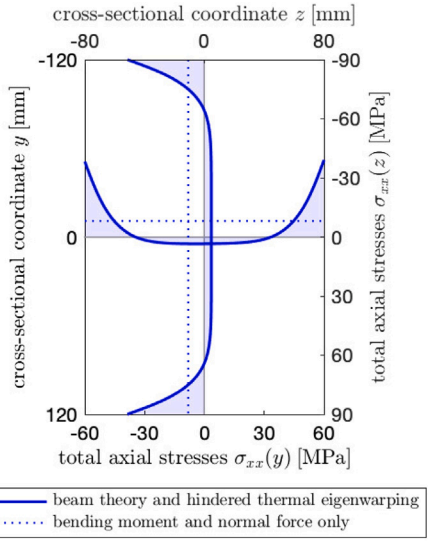

Fig. 24. Distribution of axial stresses across the cross-section of the left column at initiation of tensile cracking, 11.7 min after the start of the fire.

start of the fire, the tensile strength of concrete is reached at the axis of the columns, see Fig. 24. At that time instant, the heat front has propagated some 4 cm into the columns. An almost uniform stress state with tensile stresses near the tensile strength of concrete, prevails in the remaining central region of the columns, see Fig. 24. This explains why the crack propagates very quickly from 11.7 to 12 min after the start of the fire, up to a size which is equal to 80% of that reached 30 min after the start of the fire, see Fig. 25. This first phase of fast cracking is followed by a second phase of much slower crack propagation. The compressive normal force increases throughout the first 30 min of the fire from some 340 kN to some 400 kN, see Fig. 26 and Section 7.2 for a more detailed discussion.

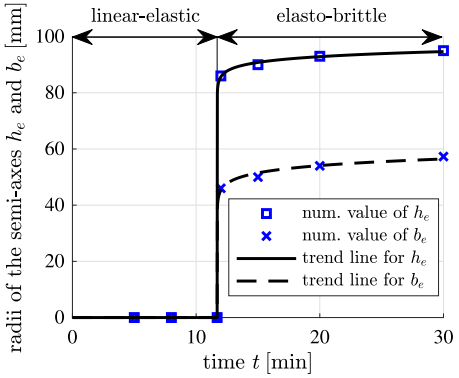

Fig. 25. Evolution of the radii of the semi-axes of the elliptic cracks, h_e and b_e, during the first 30 min after the start of the fire: the symbols denote simulation results (see also Table 8); the solid lines refer to power-law trend lines.

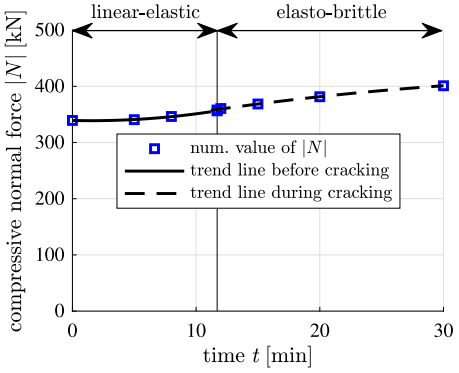

Fig. 26. Evolution of the compressive normal force of the left column during the first 30 min after the start of the fire: the squares denote simulation results computed with beam analysis software (see also Table 8); the solid and dashed lines, respectively, refer to the trend lines before and during cracking.

6. Analysis of structural variations, in terms of the cross-sectional area of the columns

In order to generalize the findings concerning tensile cracking of the columns, structural variations are studied next. In more detail, the equivalent cross-sectional area of the columns, $A_{C,eq}$, is varied from 0.6 to 1.5 times the value which was actually realized by Lu et al. (2019), the latter value amounting to 4.387×10^4 mm^2. At the same time, the h/b-ratio of the equivalent cross sections remains unaltered, as do the other geometric properties of the frame structure, the material properties of concrete and steel, and the thermo-mechanical loading. What also remains unaltered, is the reinforcement degree of the columns: it is kept fixed at $\rho = 0.02945$. The duration from the start of the fire until the initiation of tensile cracking, t_{cr}, is computed ten times, as described in Section 4, see Table 9.

Throughout the entire range of investigated equivalent cross-sectional areas, an increase of the value of $A_{C,eq}$ is always associated with an earlier occurrence of cracking. This can be explained as follows:

- With increasing values of $A_{C,eq}$, the extensional stiffness of the columns increases relative to the constant stiffness of the frame consisting of the walls and the slabs. This leads to load redistributions within the statically indeterminate structure. They manifest themselves in a moderate increase of the compressive normal force due to mechanical loads carried by the columns, $N_{C,0}$, see the second column of Table 9. However, the significant increase of the equivalent cross-sectional area outweighs the moderate increase of the compressive normal force, so that the compressive

Table 8
Input values for simulations with beam analysis software, referring to different time instants of the fire: eigenstretches and eigencurvatures are defined in Eqs. (28)-(30) and (41), the equivalent geometric properties of the cracked columns are defined in Eqs. (37)-(38).

	Top Slab	Bottom Slab	Lateral Wall	Columns	
	ϵ_0^e [−], κ_0^e [mm^{-1}]	ϵ_0^e [−], κ_0^e [mm^{-1}]	ϵ_0^e [−], κ_0^e [mm^{-1}]	ϵ_0^e [−], κ_0^e [mm^{-1}]	A_{eq} [mm^2], I_{eq} [mm^4]
$t_1 = 5$ min	$\epsilon_0^e = 0.2123 \times 10^{-5}$ $\kappa_0^e = 0.5436 \times 10^{-7}$	$\epsilon_0^e = 0.2362 \times 10^{-5}$ $\kappa_0^e = 0.6719 \times 10^{-7}$	$\epsilon_0^e = 0.1172 \times 10^{-5}$ $\kappa_0^e = 0.3575 \times 10^{-7}$	$\epsilon_0^e = 0.2904 \times 10^{-4}$ $\kappa_0^e = 0$	$A_{eq} = 4.387 \times 10^4$ $I_{eq} = 9.291 \times 10^7$
$t_2 = 8$ min	$\epsilon_0^e = 1.0781 \times 10^{-5}$ $\kappa_0^e = 2.6598 \times 10^{-7}$	$\epsilon_0^e = 1.1900 \times 10^{-5}$ $\kappa_0^e = 3.2532 \times 10^{-7}$	$\epsilon_0^e = 0.5273 \times 10^{-5}$ $\kappa_0^e = 1.5325 \times 10^{-7}$	$\epsilon_0^e = 1.3929 \times 10^{-4}$ $\kappa_0^e = 0$	$A_{eq} = 4.387 \times 10^4$ $I_{eq} = 9.291 \times 10^7$
$t_3 = 11.7$ min	$\epsilon_0^e = 2.8454 \times 10^{-5}$ $\kappa_0^e = 6.7536 \times 10^{-7}$	$\epsilon_0^e = 3.1176 \times 10^{-5}$ $\kappa_0^e = 8.1695 \times 10^{-7}$	$\epsilon_0^e = 1.6116 \times 10^{-5}$ $\kappa_0^e = 4.5273 \times 10^{-7}$	$\epsilon_0^e = 3.4902 \times 10^{-4}$ $\kappa_0^e = 0$	$A_{eq} = 4.387 \times 10^4$ $I_{eq} = 9.291 \times 10^7$
$t_3 = 12$ min	$\epsilon_0^e = 2.9903 \times 10^{-5}$ $\kappa_0^e = 7.0657 \times 10^{-7}$	$\epsilon_0^e = 3.2740 \times 10^{-5}$ $\kappa_0^e = 8.5366 \times 10^{-7}$	$\epsilon_0^e = 1.7070 \times 10^{-5}$ $\kappa_0^e = 4.7683 \times 10^{-7}$	$\epsilon_0^e = 5.7670 \times 10^{-4}$ $\kappa_0^e = 0$	$A_{eq}^{cr} = 3.144 \times 10^4$ $I_{eq}^{cr} = 8.634 \times 10^7$
$t_3 = 15$ min	$\epsilon_0^e = 4.3774 \times 10^{-5}$ $\kappa_0^e = 10.0297 \times 10^{-7}$	$\epsilon_0^e = 4.7718 \times 10^{-5}$ $\kappa_0^e = 12.0190 \times 10^{-7}$	$\epsilon_0^e = 2.9102 \times 10^{-5}$ $\kappa_0^e = 7.8817 \times 10^{-7}$	$\epsilon_0^e = 8.1324 \times 10^{-4}$ $\kappa_0^e = 0$	$A_{eq}^{cr} = 2.974 \times 10^4$ $I_{eq}^{cr} = 8.408 \times 10^7$
$t_4 = 20$ min	$\epsilon_0^e = 6.8219 \times 10^{-5}$ $\kappa_0^e = 15.0607 \times 10^{-7}$	$\epsilon_0^e = 7.4158 \times 10^{-5}$ $\kappa_0^e = 17.9003 \times 10^{-7}$	$\epsilon_0^e = 5.1733 \times 10^{-5}$ $\kappa_0^e = 13.3951 \times 10^{-7}$	$\epsilon_0^e = 11.8837 \times 10^{-4}$ $\kappa_0^e = 0$	$A_{eq}^{cr} = 2.810 \times 10^4$ $I_{eq}^{cr} = 8.141 \times 10^7$

Table 9
Results of the analysis regarding structural variations in terms of the equivalent cross-sectional areas of the columns, $A_{C,eq}$: values of the compressive normal force due to mechanical loads, $N_{C,0}$, the compressive normal force due to the thermal load 11.7 min after the start of the fire, $N_{C,\varepsilon}$, and the duration from the start of the fire until the initiation of tensile cracking, t_{cr}.

Equivalent area	Normal force		Crack time
$A_{C,eq}$ [mm^2]	$N_{C,0}$ [kN]	$N_{C,\varepsilon}$ [kN]	t_{cr} [min]
2.632×10^4	−335.0	−18.8	13.4
3.071×10^4	−336.6	−18.2	12.7
3.510×10^4	−337.8	−17.7	12.2
3.948×10^4	−338.7	−17.4	11.9
4.387×10^4	−339.4	−17.1	11.7
4.826×10^4	−340.0	−16.9	11.5
5.265×10^4	−340.5	−16.7	11.4
5.703×10^4	−340.9	−16.5	11.3
6.142×10^4	−341.2	−16.4	11.2
6.581×10^4	−341.5	−16.3	11.1

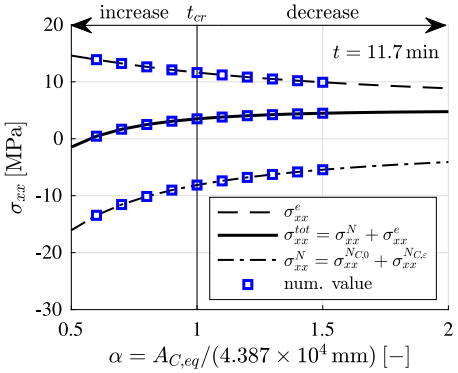

Fig. 27. Results of the analysis regarding structural variations in terms of the equivalent cross-sectional areas of the columns, $A_{C,eq}$: Evolution of the hindered-warping-induced stresses (dashed line), the total axial stresses (solid line), and the normal force related stresses (dash-dotted line), 11.7 min after the start of the fire.

axial normal stresses in the columns *decrease* with increasing value of $A_{C,eq}$.

- With the same temperature evolution being imposed at the surface of the columns with varying cross-sectional areas, the columns' thermal stretches according to Eq. (30) evolve the slower the larger the value of $A_{C,eq}$. This implies two counteracting effects: (i) The incompatibility between the thermal elongation of the columns and the deformation of the walls decreases. Therefore, the columns are pushing less against the surrounding frame consisting of slabs and walls, and the compressive normal force experienced by the columns, $N_{C,\varepsilon}$, increases more slowly, see the third column of Table 9. This effect tends to decrease the duration from the start of the fire to the initiation of tensile cracking. (ii) The hindered-warping-induced tensile stresses at the core of the columns evolve more slowly. This effect tends to increase the duration from the start of the fire to the initiation of tensile cracking.

Total tensile stresses at the center of the column increase with increasing cross-sectional area, see the thick solid line in Fig. 27. This results from a significant reduction of the compressive normal force induced stresses (dash-dotted line) and a moderate reduction of the hindered-warping-induced tensile stresses (dashed line).

7. Discussion

7.1. Stress redistributions due to tensile cracking

It is interesting to discuss redistributions of stress resultants and changes of stresses induced by tensile cracking of the left column. To this end, results from two simulations are compared. They are performed with and without consideration of tensile cracking and they refer to 30 min after the start of the fire.

The eigenstretch of the cracked left column is by 36% larger than the value obtained without consideration of tensile cracking (Table 10). This change results from the fact that the average temperature in the outer intact part of the column is by 36% higher than the average temperature of the entire cross-section.

The extensional stiffness of the cracked left column is by 39% smaller than the value obtained without consideration of cracking, see Table 10. This change results from the fact that cracking reduces the equivalent area of the cross-section by 39%, see Eq. (37).

As regards the normal force experienced by the left column, the larger eigenstretch and the smaller extensional stiffness result in two competing effects:

- Because of the larger thermal eigenstretch, the columns expand more and could be expected to push even stronger against the slabs. This effect tends to increase the compressive normal force carried by the columns.
- Stiffer elements of a statically indeterminate structure attract a larger share of the load than less stiff elements. Because of the reduced stiffness of the columns, this effect tends to redistribute the stress resultants towards the stiffer walls, decreasing the expected compressive normal force carried by the columns.

The described structural analysis clarifies that the former effect slightly outperforms the latter: the compressive normal force carried by the left column increases, because of cracking, by only some 2.3% from

Table 10
Cracking-induced changes of properties of the left column, its normal force, and stresses experienced by concrete.

Property	Intact	Cracked (change)
Equivalent area	43870 mm^2	26673 mm^2 (−39%)
Extensional stiffness	1465 kN	891 kN (−39%)
Eigenstretch	13.7×10^{-4}	18.6×10^{-4} (+36%)
Normal force	−391.8 kN	−401.0 kN (+2.3%)
Stresses associated with normal forces and bending moments	−8.9 MPa	−15.0 MPa (+68.5%)
Maximum hindered-warping-induced compressive stresses	−39.8 MPa	−23.6 MPa (−40.7%)
Maximum compressive total stresses	−47.5 MPa	−38.6 MPa (−18.7%)

−391.8 kN to −401.0 kN, see Table 10. Thus, the redistributions of the stress resultants, resulting from tensile failure of concrete at the core of the left column, are rather insignificant, compare Fig. 17 with Fig. 22.

The beam-theory-related stresses resulting from a slightly increased compressive normal force and a significantly reduced cross-sectional area, are by some 68.5% larger than the values obtained without consideration of cracking, see Table 10. They increase from −8.9 MPa (without cracking, see Fig. 18) to −15.0 MPa (with cracking, see Fig. 23).

Hindered-warping-induced stresses remain *qualitatively the same* in the intact outer region of the cracked column, compare Figs. 14 and 21, but they are equal to zero in the cracked core region. Because the hindered-warping-induced stresses are self-equilibrated, the integral over the remaining hindered-warping-induced stresses must vanish, such that they do not contribute to the normal force. Thus, the hindered-warping-induced stresses change quantitatively: at the outer contour of the cross-section, they decrease from −39.8 MPa (without cracking, see Fig. 14) to −23.6 MPa (with cracking, see Fig. 21). The reduction of the hindered-warping-induced stresses, resulting from cracking of concrete is sometimes referred to as "reduction of the constraint of the reinforced concrete member", see e.g. (El-Tayeb et al., 2017).

Total stresses are the sum of the hindered-warping-induced stresses and the stresses associated with normal forces and bending moments. At the outer contour of the left column, the total stresses decrease from −47.5 MPa (without cracking, see Fig. 18) by 18.7% (see Table 10) to −38.6 MPa (with cracking, see Fig. 23). This change is governed by cracking-induced changes regarding the hindered-warping-induced stresses.

Finally, it is noteworthy that the compressive stress of concrete was equal to −7.7 MPa at half-height of the left column *before* the start of the fire. This stress increased, during the first 30 min of the fire, by almost 400% to −38.6 MPa, which is virtually equal to the 28-days compressive strength of the concrete (Díaz et al., 2018).

7.2. Behavior of reinforced concrete columns during a fire

The finding that the core regions of the columns were damaged can be generalized from the here-analyzed statically indeterminate frame structure to other reinforced concrete structures. Corresponding arguments refer to changes of the compressive normal forces experienced by the columns, resulting from the fire loading and from tensile cracking, respectively:

- In the here-analyzed statically indeterminate frame structure, fire loading increased the compressive normal force of the columns from some 340 kN to some 400 kN, because of the following two reasons: 1. The columns were heated more than the walls and slabs. This led to larger eigenstretches in the columns, and smaller eigenstretches in the walls. 2. The larger eigenstretches of the columns were constrained by the statically indeterminate frame structure surrounding them. This led to an increase of the compressive normal forces experienced by the columns, see Fig. 26. Still, this increase of compression could not prevent the columns from tensile cracking in their core regions, see Fig. 25.
- In statically determinate structures, compressive normal forces experienced by columns are independent of fire loading, because they are controlled by equilibrium only. Therefore, it is even more likely that statically determinate columns will suffer from tensile cracking in their core regions, compared to the here-studied case.
- Herein, core-cracking of the columns was shown to result in an increase of the compressive normal forces of the columns by some 3% only. This is reminiscent of statically determinate structures, where partial cracking of a reinforced concrete column has no influence on its normal force. Thus, the cracking-related stress redistributions inside the here-analyzed column are similar to those found in other reinforced concrete structures.

Fire-loaded columns undergo a sequence of characteristic processes during the initial phase of the fire, the high-temperature situation, and after the fire.

In the initial phase of the fire, transient heat conduction results in non-linear temperature profiles. The outer surface is already hot, while the core is still rather cool. Corresponding hindered-warping-induced stresses are compressive in the outer region and tensile in the core region of the columns. While temperatures are not yet high enough to significantly reduce the stiffness and strength of concrete, the hindered-warping-induced stresses increase the total compressive stresses at the outer contour of the columns, and decrease them in the core region around the axis of the columns. As shown in the presented example, it is likely that hindered-warping-induced stresses will give rise to tensile stresses at the core of the columns, see also (Elbadry and Ghali, 1986; Vecchio and Sato, 1990). Once they reach the tensile strength of concrete, the core region of the columns will crack. It is likely that this will occur unnoticed during fire testing, unless there are build-in sensors measuring the axial normal stresses and possible cracking at the core of the columns.

During the main phase of the fire, with temperatures rising up say 1000 °C, dehydration of concrete and associated effects (Ulm et al., 1999b,a) reduce the stiffness (and strength) of concrete, particularly so in the region of the heated surface of the columns. More compliant concrete close to the surface exhibits stress relaxation. This process results in the re-distribution of compressive stresses from the outer to the inner region of the columns, where concrete is still much stiffer (Ali et al., 2010). Thus, cracks that have appeared during the first phase of the fire will close during the main phase of the fire.

After the fire, when the columns cool down, transient heat conduction changes its direction. The core of the columns is warmer than their surfaces. Corresponding hindered-warping-induced stresses are tensile in the outer region and compressive in the core region of the columns. Thus, also during cooling damage of columns is expected to progress, see also (Ožbolt et al., 2014; Molkens, 2022).

8. Conclusions

Three-dimensional nonlinear thermo-mechanical FE simulations of the fire test by Lu et al. (2019) and a beam-theory-related analysis delivered very similar results regarding internal cracking of the

columns. This is remarkable because the FE simulation accounted for temperature-dependent thermo-mechanical properties and non-linear stress–strain relations of concrete and steel, while the beam-theory-based analysis was based on temperature-independent thermo-mechanical properties and linear stress–strain relations, except for concrete subjected to tension, which was idealized to exhibit linear elastic behavior followed by sudden brittle failure. The results suggest the following conclusions:

- Model reduction allowed for a speed-up of the structural analysis by a factor of 500.
- The modular beam-theory-based approach delivers a continuous (rather than discretized) resolution of non-linear stress distributions.
- Temperature-dependent thermo-mechanical properties of concrete and steel (including the thermal diffusivity, the elastic stiffness, pre-peak non-linearities of stress–strain diagrams, and the tensile strength) are only of secondary importance when it comes to stress states inside columns subjected to a moderate fire which lasts for 30 min and leads to a maximum surface temperature of 300 degrees centigrade.
- Hindered-warping-induced stresses, which are compressive in near-surface regions and tensile in the vicinity of the axis of the columns, are first-order effects. They result in tensile cracking of the core of the compressed columns already 11 min after the start of the fire, during which the surface temperature increased from 20 to 170 °C.
- Even if a fire can be extinguished quickly, and even if no significant damage can be detected at the fire-exposed surface of a reinforced concrete column, it is very likely that it got damaged nonetheless.

Declaration of competing interest

The authors declare that they have no known competing financial interests or personal relationships that could have appeared to influence the work reported in this paper.

Data availability

Data will be made available on request.

Acknowledgments

The authors gratefully acknowledge project FFG-COMET #882504 “Rail4Future: Resilient Digital Railway Systems to enhance performance", TU Wien Bibliothek, Austria for financing of open access publication, and interesting discussions with Dr. Mehdi Aminbaghai (TU Wien) regarding beam analysis software.

References

Albrifkani, S., Wang, Y.C., 2016. Explicit modelling of large deflection behaviour of restrained reinforced concrete beams in fire. Eng. Struct. 121, 97–119.
Ali, F., Nadjai, A., Choi, S., 2010. Numerical and experimental investigation of the behavior of high strength concrete columns in fire. Eng. Struct. 32, 1236–1243.
Bratina, S., Čas, B., Saje, M., Planinc, I., 2005. Numerical modelling of behaviour of reinforced concrete columns in fire and comparison with Eurocode 2. Int. J. Solids Struct. 42, 5715–5733.
Choi, E., Shin, Y., 2011. The structural behavior and simplified thermal analysis of normal-strength and high-strength concrete beams under fire. Eng. Struct. 33, 1123–1132.
Dassault Systemes Simulia Corp, 2019. ABAQUS CAE.
Díaz, R., Wang, H., Mang, H., Yuan, Y., Pichler, B., 2018. Numerical analysis of a moderate fire inside a segment of a subway station. Appl. Sci. 8, 2116.
Dlubal Software GmbH, 2020. RStab (8.22).
El-Tayeb, E.H., El-Metwally, S.E., Askar, H.S., Yousef, A.M., 2017. Thermal analysis of reinforced concrete beams and frames. HBRC J. 13, 8–24.
Elbadry, M., Ghali, A., 1986. Thermal stresses and cracking of concrete bridges. ACI Struct. J. 83, 1001–1009.
Elishakoff, I., 2020. Who developed the so-called Timoshenko beam theory? Math. Mech. Solids 25, 97–116.
Gao, W., Dai, J.G., Teng, J., Chen, G., 2013. Finite element modeling of reinforced concrete beams exposed to fire. Eng. Struct. 52, 488–501.
Han, L.H., Zheng, Y.Q., Tao, Z., 2009. Fire performance of steel-reinforced concrete beam–column joints. Mag. Concr. Res. 61, 499–518.
International Organization for Standardization (ISO), 1999. ISO 834-1:1999 fire resistance test – elements of building construction – part 1: general requirements.
Kodur, V., Cheng, F.P., Wang, T.C., Sultan, M., 2003. Effect of strength and fiber reinforcement on fire resistance of high-strength concrete columns. J. Struct. Eng. 129, 253–259.
Kodur, V., Raut, N., Mao, X., Khaliq, W., 2013. Simplified approach for evaluating residual strength of fire-exposed reinforced concrete columns. Mater. Struct. 46, 2059–2075.
Kodur, V., Wang, T., Cheng, F., 2004. Predicting the fire resistance behaviour of high strength concrete columns. Cem. Concr. Compos. 26, 141–153.
Kodur, V., Yu, B., Solhmirzaei, R., 2017. A simplified approach for predicting temperatures in insulated RC members exposed to standard fire. Fire Saf. J. 92, 80–90.
Lie, T., Erwin, R., 1993. Method to calculate the fire resistance of reinforced concrete columns with rectangular cross section. ACI Struct. J. 90, 52–60.
Lu, L., Qiu, J., Yuan, Y., Tao, J., Yu, H., Wang, H., Mang, H., 2019. Large-scale test as the basis of investigating the fire-resistance of underground RC substructures. Eng. Struct. 178, 12–23.
Molkens, T., 2022. The cooling phase, a key factor in the post-fire performance of RC columns. Fire Saf. J. 128, 103535.
Öchsner, A., 2021. Classical Beam Theories of Structural Mechanics. Springer International Publishing.
Ožbolt, J., Bošnjak, J., Periškić, G., Sharma, A., 2014. 3D numerical analysis of reinforced concrete beams exposed to elevated temperature. Eng. Struct. 58, 166–174.
Özısık, M.N., 1993. Heat Conduction. John Wiley & Sons.
Ring, T., Zeiml, M., Lackner, R., 2014a. Underground concrete frame structures subjected to fire loading: Part I–large-scale fire tests. Eng. Struct. 58, 175–187.
Ring, T., Zeiml, M., Lackner, R., 2014b. Underground concrete frame structures subjected to fire loading: Part II–re-analysis of large-scale fire tests. Eng. Struct. 58, 188–196.
Sorgner, M., Díaz Flores, R., Wang, H., Pichler, B.L.A., 2022. Engineering mechanics analysis of a moderate fire inside a segment of a subway station. In: Proceedings of the Conference on Computational Modelling of Concrete and Concrete Structures. EURO-C 2022, pp. 239–246.
Terro, M.J., 1998. Numerical modeling of the behavior of concrete structures in fire. ACI Struct. J. 95, 183–193.
Ulm, F.J., Acker, P., Lévy, M., 1999a. The “Chunnel” fire. II: Analysis of concrete damage. J. Eng. Mech. 125, 283–289.
Ulm, F.J., Coussy, O., Bažant, Z.P., 1999b. The “Chunnel” fire. I: Chemoplastic softening in rapidly heated concrete. J. Eng. Mech. 125, 272–282.
Vecchio, F.J., Sato, J., 1990. Thermal gradient effects in reinforced concrete frame structures. ACI Struct. J. 87, 262–275.
Wang, H., Höller, R., Aminbaghai, M., Hellmich, C., Yuan, Y., Mang, H.A., Pichler, B.L., 2019. Concrete pavements subjected to hail showers: A semi-analytical thermoelastic multiscale analysis. Eng. Struct. 200, 109677.
Wang, H., Yuan, Y., Mang, H.A., Ai, Q., Huang, X., Pichler, B.L., 2022. Thermal stresses in rectangular concrete beams, resulting from constraints at microstructure, cross-section, and supports. Eur. J. Mech. A Solids 93, 104495.
Xu, Y.y., Wu, B., 2009. Fire resistance of reinforced concrete columns with L-, T-, and +-shaped cross-sections. Fire Saf. J. 44, 869–880.
Zha, X., 2003. Three-dimensional non-linear analysis of reinforced concrete members in fire. Build. Environ. 38, 297–307.